

Article

Structure and Martensitic Transformation in Rapidly Solidified CoNiAlFe Alloy

Huiling Chen ¹, Jia Ju ^{1,2,3,*}, Ligu Shuai ^{1,*}, Huan Liu ⁴ , Chen Yan ⁵ and Zhuang Liu ²

¹ School of Mechanical Engineering, Southeast University, Nanjing 211189, China; fchhl@163.com

² Jiangsu Key Laboratory of Advanced Structural Materials and Application Technology, School of Materials Engineering, Nanjing Institute of Technology, Nanjing 211167, China; putiyishu@gmail.com

³ Hangzhou Kaiierda Electric Welder Co., Ltd., Hangzhou 310000, China

⁴ College of Mechanics and Materials, Hohai University, Nanjing 211100, China; liuhuanseu@hhu.edu.cn

⁵ Zhongtian Alloy Technology Co., Ltd., Nantong 226010, China; yanchen@chinaztt.com

* Correspondence: materialju@njit.edu.cn (J.J.); ligu.shuai@126.com (L.S.);
Tel.: +86-181-5100-7171 (J.J.); +86-138-1389-3943 (L.S.)

Received: 19 September 2017; Accepted: 31 October 2017; Published: 3 November 2017

Abstract: Housler based magnetic controlled shape memory alloys are characterized by a large magnetic field induced strain. The strain was dependent on the twin martensite structure rearrangement, and the rapid solidification technology had a significant influence on the microstructure, physical, and chemical properties of the alloy. Thus, the structure and the martensitic transformation changes of $\text{Co}_{33}\text{Ni}_{31}\text{Al}_{27}\text{Fe}_9$ during the rapidly solidified process were studied. The microstructure of $\text{Co}_{33}\text{Ni}_{31}\text{Al}_{27}\text{Fe}_9$ with furnace cooled and rapid solidification (RS) constitutes a dual-phase structure, β phase and γ phase in a low cooling rate and martensite and γ phase in a high cooling rate. The γ phase at the grain boundaries reduced and became more fragile by raising the R_C value. The one-step austenite-martensite phase transformation occurred during the process of heating and cooling. The phase transition temperature presents an increasing trend by rising the cooling rate, even to over the room temperature. Moreover, the martensite structure in $\text{Co}_{33}\text{Ni}_{31}\text{Al}_{27}\text{Fe}_9$ constitutes a typical $L1_0$ -type twinning structure.

Keywords: structure; twin martensite; phase transformation; housler alloy; CoNiAlFe

1. Introduction

In the past three decades, Housler based magnetic controlled shape memory alloys (MCMEA), such as Ni-Mn-Ga [1,2], Co-Ni-Ga [3,4], Ni-Fe-Ga [5,6], Ni-Mn-X (X = In, Sb, Al) [7,8], and Co-Ni-Al [9,10], have attracted much scientific attention as it concerns the sensors and actuators industry. These kinds of Housler alloys are characterized by the ability of creating a large magnetic field induced strain (MFIS) and their high response frequency under an external magnetic field (EMF) [11,12].

Among these Housler alloys, the Co-Ni-Al system represents a new kind of MCMEA since the first order martensitic transformation from a high temperature paramagnetic cubic austenite phase to a low temperature ferromagnetic tetragonal twin martensitic phase was observed by Oikawa in Co-Ni-Al alloy [13]. Additionally, recent studies [10,14,15] on Co-Ni-Al series alloys, revealed that a large output MFIS could be affected by two main parameters, including a suitable martensite structure and a large deformation drive force. As it concerns the first factor, the MFIS can be obtained due to the martensite twin boundaries rearrangement under EMF. This is due to the magnetic domains, which exist in twin martensite variants, migrated in parallel with EMF direction, which results in the martensite variants being rearranged. In addition, as it concerns the second factor, the drive force

for MFIS can be controlled by saturation magnetization and magnetocrystalline anisotropy of alloy, as described by Handley [16] and Ju et al. [14].

Nevertheless, there are many techniques to obtain a suitable martensite structure and the large deformation drive force, such as alloying, heat treatment, rapid solidification (RS), and directional solidification [17,18]. For these techniques, RS, including suction casting and injection, represent one of important non-equilibrium processing technique, and it has been frequently employed to change the microstructure and enhance the alloy properties. When compared to conventional solidification (CS), RS demonstrates a higher cooling rate (R_C , approximately $1 \times 10^4 \text{ K}\cdot\text{s}^{-1}$) than CS (less than $50 \text{ K}\cdot\text{s}^{-1}$), and this results on the microstructure, as long as on the physical and chemical properties of alloy, which present a significant change during RS processes [18–20].

In the current paper, the authors focused on the martensitic transformation changes of typical MCMEA $\text{Co}_{33}\text{Ni}_{31}\text{Al}_{27}\text{Fe}_9$ (this alloy established apparent MSIF under EMF) during rapidly solidified process. In particular, the changes of martensite structure, martensitic transformation temperature, and the thermal hysteresis during rapidly solidified process were investigated in detail. Moreover, the relationship between martensitic transformation and different cooling rate was defined.

2. Materials and Methods

MCMEA samples with the nominal composition $\text{Co}_{33}\text{Ni}_{31}\text{Al}_{27}\text{Fe}_9$ were prepared by high-pure metals (the purity of Co, Ni, Al, and Fe was more than 99.99%, produced by China New Metal Materials Technology Co., Ltd., Beijing, China) using an arc-melting furnace (WK II, SKY Technology Development Co., Ltd., Shenyang, Liaoning, China) at 1973 K in an inert atmosphere (pure argon). Then, both CS (CS process was carried out by furnace cooled) and RS (RS process was carried out by suction cast in water cooled thick copper mold and the size of samples after suction cast were $1 \text{ mm} \times 70 \text{ mm}$, $4 \text{ mm} \times 70 \text{ mm}$, $8 \text{ mm} \times 70 \text{ mm}$ (diameter \times length)) process were carried out. To avoid the melting loss, the high-pure metals with high melting point, like Co, Ni, and Fe, were prepared 5 % more. The high-pure metals with a low melting point, like Al, were prepared 15 % more. Annealing sample was carried out at 1400 K for 6 h with an inert atmosphere (pure argon).

The relation between R_C and suction cast diameter were determined according to the Equation (1) as suggested by Johnson [21] and Liu [20], and the R_C values were calculated as listed in Table 1:

$$R_c = \frac{4000}{d^2} \quad (1)$$

Table 1. R_C values during rapid solidification (RS) techniques.

Alloy	Diameter (mm)	R_C ($\text{K}\cdot\text{s}^{-1}$)
D1	1	4000
D4	4	250
D8	8	62.5

The microstructure morphology and the element distribution of samples were examined by FEI-Sirion200 type scanning electron microscopy (SEM, FEI, Hillsboro, OR, USA), equipped with an energy-dispersive X-ray spectrometry (EDS, Field Electron and Ion Company, Hillsboro, OR, USA) microanalysis system. The crystallographic phase identification was carried out by Philips PW170 type X-ray diffraction (XRD, Philips, Amstel dam, The Netherlands), with $\text{CuK}\alpha$ radiation source ($\lambda = 1.5418 \text{ \AA}$) in the 2θ range between 10° – 90° . For fine bar shaped samples, a special testing mold (as seen in Figure 1) was used during the XRD test. The structure of martensite was determined by JOEL-2000EX type transmission electron microscopy (TEM, JOEL, Tokyo, Japan), and selected area electron diffraction patterns (SADP). Finally, the martensitic transformation temperature and thermal hysteresis of samples were analyzed by STA449 F3 type differential scanning calorimeter (DSC, Netzsch, Bavarian, Germany) and selected area electron diffraction patterns (SADP). Finally,

the martensitic transformation temperature and thermal hysteresis of samples were analyzed by STA449 at the cooling and heating rate of $5 \text{ K}\cdot\text{min}^{-1}$.

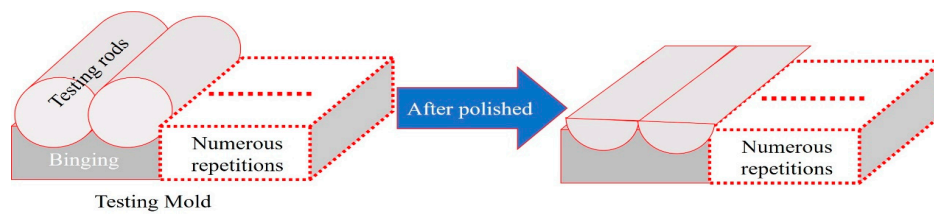


Figure 1. Schematic diagram of the X-ray diffraction (XRD) testing mold.

3. Results

3.1. Microstructure

For MCMEA, a suitable microstructure constitutes one of the conditions to obtain MFIS and the microstructure can be formed by solidification processes and element composition [17]. Figure 2 demonstrates the microstructure detail of $\text{Co}_{33}\text{Ni}_{31}\text{Al}_{27}\text{Fe}_9$ alloy with furnace cooled and RS processes. For the furnace cooled sample (Figure 1a), a typical dual-phases structure consisted of the dark color parent phases, while the light color secondary phases can be observed. The secondary phases presented a continuous distribution and gathered in grain boundaries (the red circle in Figure 2a). For the RS sample, the microstructure of the sample with a lower R_C value, preserved the light color secondary phases surrounding the dark color parent phases dual-phase structure, as seen in Figure 2b. However, the only difference is that the secondary phases no longer present a tendency to aggregate at the grain boundaries. By increasing the R_C value, a significant change of microstructure occurred in the sample. The dark color parent phases vanished and were replaced by lath-shaped phases. Meanwhile, the light color continuous distribution secondary phases changed into fragmentary type at the grain boundaries as illustrated in Figure 2c. For the highest R_C value, the lath-shaped phases represent the higher percentage of the area in Figure 2d. The light color secondary phases was further broken into smaller parts. After annealing, the sample consisted of both the parent phases and the secondary phases as seen in Figure 1e, which is identical to the microstructure of the sample with furnace cooled.

In order to obtain the difference between the desired composition and the actual composition of the sample, the ICP-MS test was carried out and the results list in Table 2. Actually, there is only a small error between the desired composition and the actual composition of the sample from Table 2. Each actual composition of the sample, including Furnace cooled, D8, D4, and D1, were very close to the $\text{Co}_{33}\text{Ni}_{31}\text{Al}_{27}\text{Fe}_9$.

Table 2. The difference between the desired composition and the actual composition of the sample.

Alloy	Desired Composition (at %)	Actual Composition (at %)
Furnace cooled	$\text{Co}_{33}\text{Ni}_{31}\text{Al}_{27}\text{Fe}_9$	$\text{Co}_{33.1}\text{Ni}_{31.5}\text{Al}_{26.8}\text{Fe}_{8.6}$
D8		$\text{Co}_{32.8}\text{Ni}_{31.4}\text{Al}_{27.3}\text{Fe}_{8.5}$
D4		$\text{Co}_{33.4}\text{Ni}_{30.2}\text{Al}_{28.1}\text{Fe}_{8.3}$
D1		$\text{Co}_{32.9}\text{Ni}_{32.4}\text{Al}_{26.3}\text{Fe}_{8.4}$

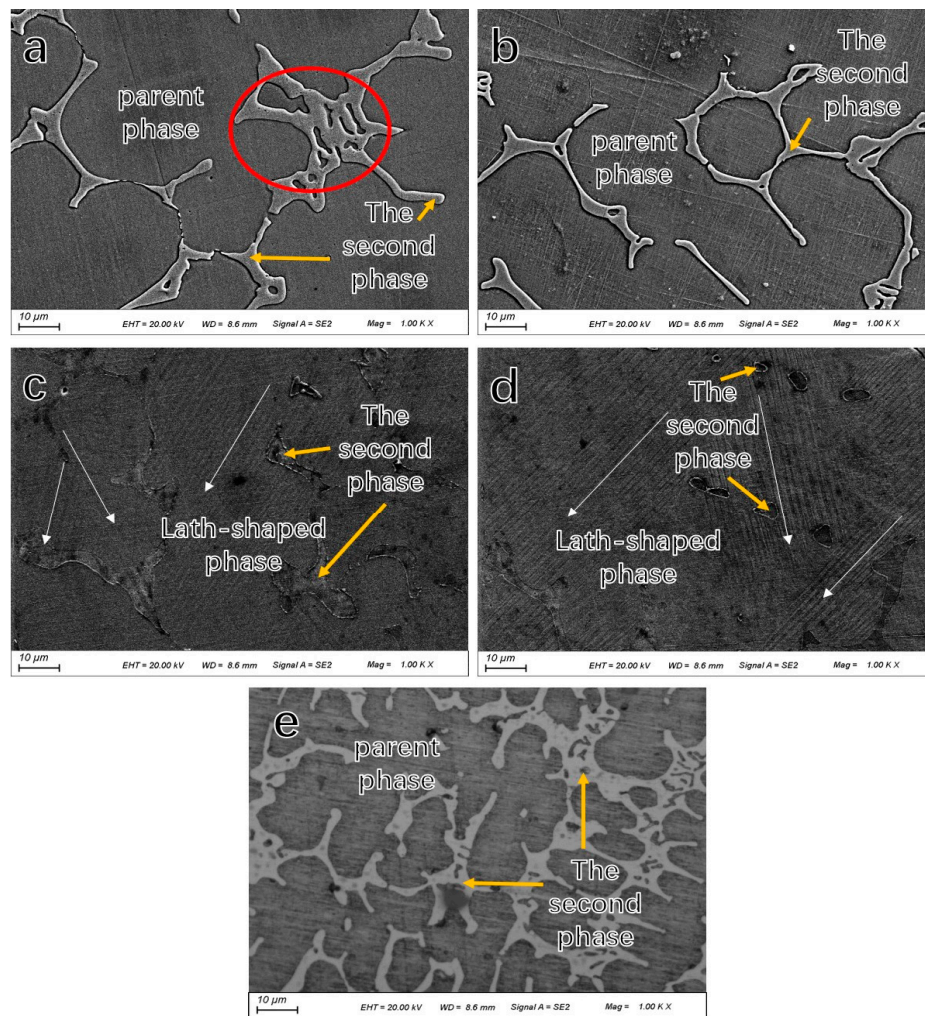


Figure 2. Morphology of microstructures in $\text{Co}_{33}\text{Ni}_{31}\text{Al}_{27}\text{Fe}_9$ alloy with furnace cooled and rapid solidification (RS): (a) furnace cooled; (b) D8; (c) D4; (d) D1; and (e) the sample after annealing.

To check the homogeneity and element distribution of final composition, EDS analysis of each sample has been carried out and the results are presented in Figure 3. The total scan area (yellow area in Figure 3) results confirm that the melting loss remained within reasonable limits and the composition of the sample (32.89~33.76 at % Co-30.30~32.54 at % Ni-25.10~27.66 at % Al-8.28~9.47 at % Fe) had a good agreement with the nominal compositions (33 at % Co-31 at % Ni-27 at % Al-9 at % Fe). Furthermore, the element distribution at different phases (the present phase, the secondary phase and the lath-shaped phase) of samples was also defined. The present phases (red area in Figure 3) of the furnace cooled sample and D8 (with lower R_C value) were found to include the same atomic ratio of elements Co, Ni, and Al (approximates to 1:1:1), but only a limited amount of element Fe. By comparing the secondary phases in furnace cooled sample and D8, they contain a high amount of element Co and Fe and less element Ni and Fe. When the R_C reached a higher value (D4 and D1), a significant trend of elemental reduction of Co and Fe content in the secondary phases appeared. Additionally, the Co and Fe content in the lath-shaped phase maintain an increasing trend with R_C being a rising value. This indicated that the elements of Co and Fe can gradually move towards the matrix when the R_C value increases. EDS line scanning of lath-shaped phase was shown in Figure 3e. As can be seen that Co, Ni, Al, and Fe content was stable in whole lath-shaped phase, indicated that the elements in lath-shaped phase were in homogeneous distribution.

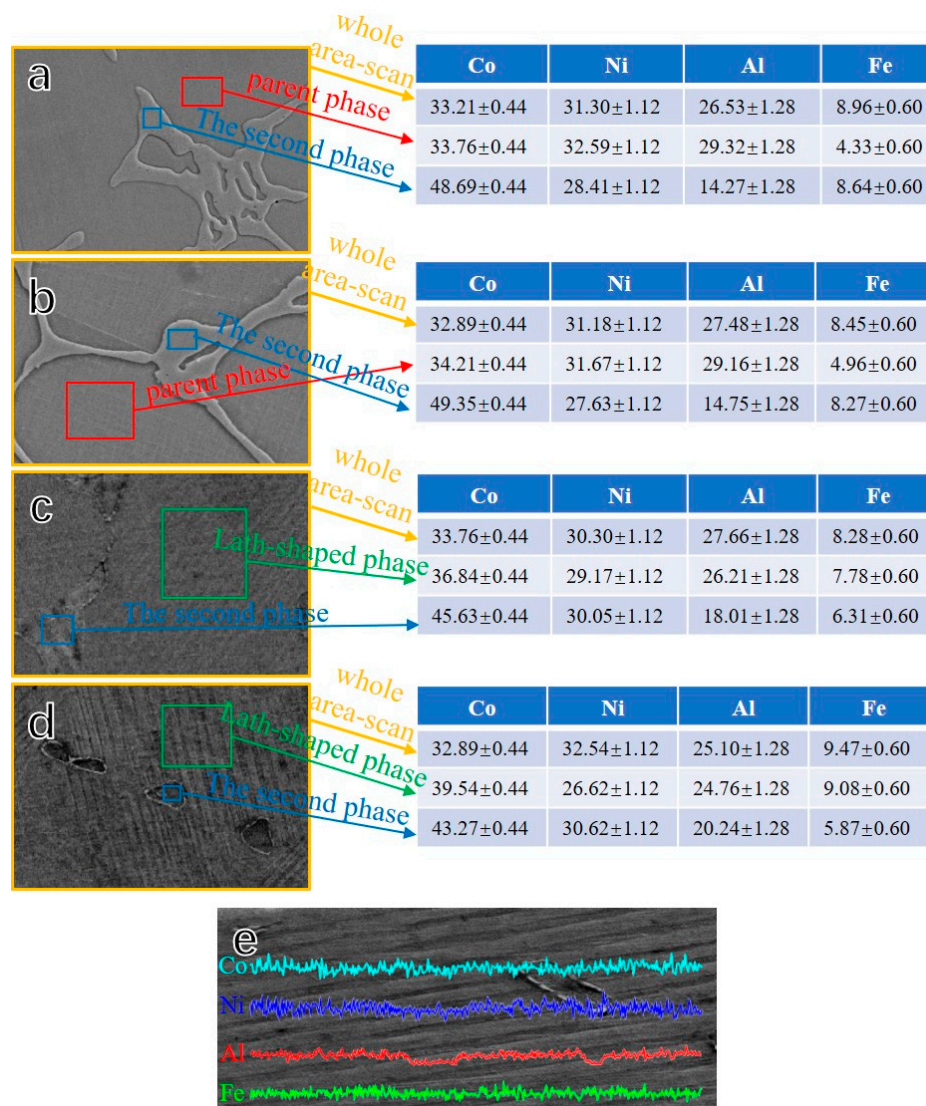


Figure 3. The X-ray spectrometry test of of the $\text{Co}_{33}\text{Ni}_{31}\text{Al}_{27}\text{Fe}_9$ alloy with furnace cooled and RS: (a) furnace cooled; (b) D8; (c) D4; (d) D1; (e) EDS line scanning of lath-shaped phase.

The XRD patterns of the $\text{Co}_{33}\text{Ni}_{31}\text{Al}_{27}\text{Fe}_9$ alloy with furnace cooled and RS at room temperature are illustrated in Figure 4. It is demonstrated that there were two phases in both the furnace cooled and RS samples, including β and γ phase in furnace cooled sample and D8, martensite and γ phase in D4 and D1, which has a good agreement with the observed in SEM analysis. The main diffraction peaks of furnace cooled sample (Figure 4a) were located at 35.6° , 48.3° , 56.1° , 70.6° , 74.8° , and 86.9° , were indexed in β phase (B2 structure) and γ phase (A1 structure) mixture. Furthermore, some peaks were sharp presenting high intensity. In the RS process with a lower R_C value (Figure 4b), there were still two phases (β phase + γ phase) including some sharp peaks, and high intensity was observed at the same degrees. When combined with SEM analysis, it can be deduced that B2 structure β phase and A1 structure γ phase should correspond to the present and the secondary phase, respectively. When the R_C value increased further (Figure 4c), the peaks for β phase disappeared. Nevertheless, some new peaks, which indexed to $L1_0$ structure martensite phase and γ phase, arose at 43.2° , 48.3° , 49.8° , 57.1° , 67.5° , and 74.8° , indicated that the lath-shaped phase, which was observed in Figure 1c,d, could be the martensite. When the R_C value reached the maximum (Figure 4d), the sample maintained a mixture of the martensite phase and γ phase and the diffraction peak appeared the broad scattering peaks. Moreover, a cubic β phase was detected at room temperature, demonstrating that the martensitic

transformation should have occurred below room temperature (in the furnace cooled sample and D8). Conversely, the tetragonal martensite phase was discovered at room temperature, indicating that the martensitic transformation occurred above room temperature (in D4 and D1).

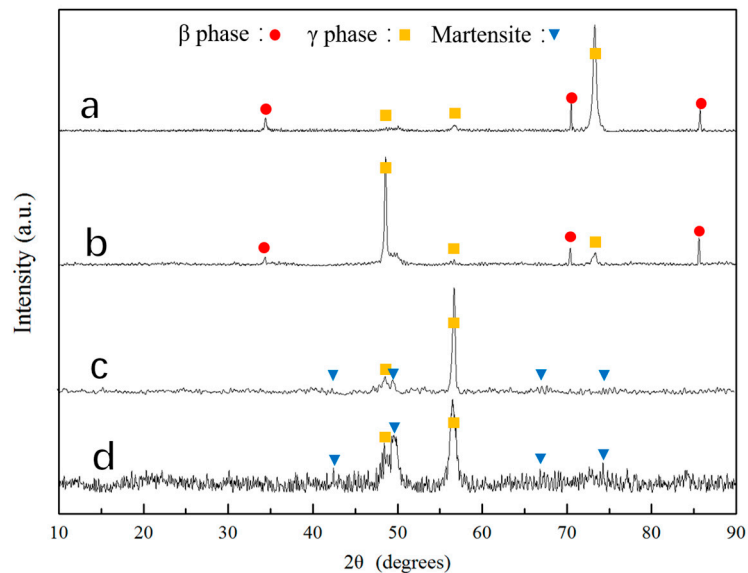


Figure 4. Room temperature XRD patterns of the $\text{Co}_{33}\text{Ni}_{31}\text{Al}_{27}\text{Fe}_9$ alloy with furnace cooled and RS: (a) furnace cooled; (b) D8; (c) D4; and (d) D1.

Usually, the morphology of microstructures and elemental distribution are sensitive to the solidification process, including the solidification mode and solidification condition [18]. The experimental conditions and the obtained phases of the $\text{Co}_{33}\text{Ni}_{31}\text{Al}_{27}\text{Fe}_9$ alloy with furnace cooled and RS are shown in Table 2. According to the data in Table 3, the solidification process depends on the R_C value, which can be represented by the model illustrated in Figure 5. In this figure, the solidification process of MCMEA can be divided into three classes when the R_C fluctuates from low to high values.

Table 3. The experimental conditions and obtained phases of $\text{Co}_{33}\text{Ni}_{31}\text{Al}_{27}\text{Fe}_9$ alloy with furnace cooled and RS.

Alloy	Experimental Conditions				Obtained Phases
	Temperature (K)	Diameter (mm)	R_C ($\text{K}\cdot\text{s}^{-1}$)	R_C Degree	
Furnace cooled	1800	-	<50	Low R_C value	$\beta + \gamma$
D8	1800	8	62.5	Low R_C value	$\beta + \gamma$
D4	1800	4	250	Medium R_C value	martensite + γ
D1	1800	1	4000	High R_C value	martensite + γ

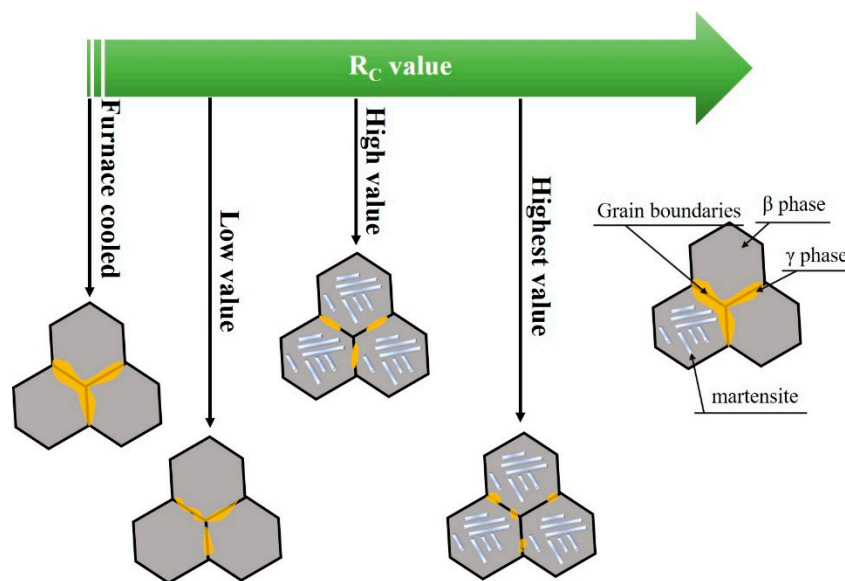


Figure 5. The schematic of the microstructural changes during the various RS processes.

Analysis of the first class (low R_C value, $R_C < 100 \text{ K}\cdot\text{s}^{-1}$):

At the solidification in a low R_C value, similar furnace cooled sample and D8, the liquid state alloy has more available time to solidify, and the secondary phase has more available time to precipitate at the grain boundaries. Thus, the microstructure appears the continuous secondary phase surrounding the parent phase. As the R_C value slightly rose (D8), the secondary phase at the grain boundaries became refined due to less available solidification time in D8.

Analysis of the second class (medium R_C value, $100 \text{ K}\cdot\text{s}^{-1} < R_C < 1000 \text{ K}\cdot\text{s}^{-1}$):

When the R_C corresponded to a medium value, the liquid state alloy obtained a high super-cooling during solidification process and the secondary phase re-melting and fragmenting occurred, by the mechanism of RS fragmenting. On the contrary, a higher solidification speed can reduce the solidification time during solidification process and result in less creation of the secondary phase at the grain boundaries.

Analysis of the third class (high R_C value, $R_C > 1000 \text{ K}\cdot\text{s}^{-1}$):

When the R_C value increases above $1000 \text{ K}\cdot\text{s}^{-1}$, during the solidification process, the third-class form occurred. A higher degree of super-cooling further intensified the secondary phase re-melting and fragmenting into a smaller part. On the contrary, the short solidification time is responsible for the reduced secondary phases arising in the alloy.

3.2. Martensitic Transformation

According to the XRD analysis, the temperature for the DSC scans of furnace cooled sample and D8 should be heating from below room temperature to test for the martensitic transformation temperature. Likewise, for D4 and D1, the temperature for DSC scans should be heating from room temperature. Figure 6 corresponds to the DSC curve of $\text{Co}_{33}\text{Ni}_{31}\text{Al}_{27}\text{Fe}_9$ alloy, including furnace cooled and RS. It is demonstrated that only one distinct endothermic and exothermic peak of DSC curve occurred during the heating and cooling processes. Thus, the phase transformation was a typical one-step phase transformation during heating and cooling. The austenite-martensite phase transformation temperature [martensite start temperature (T_{Ms}), martensite finish temperature (T_{Mf}), austenite start temperature (T_{As}), and austenite finish temperature (T_{Af})] were analyzed by the tangent method from DSC curves. The phase transformation temperature of the sample with a lower R_C value (such as furnace cooled sample and D8) was below the room temperature ($\leq 300 \text{ K}$). The sample with the increased R_C value, presented a phase transformation temperature close to the room temperature

(D4), even when higher than the room temperature (D1). For MCMEA, a higher phase transformation temperature (over room temperature) could significantly promote the application of this alloy in the field of the sensors and actuators industry.

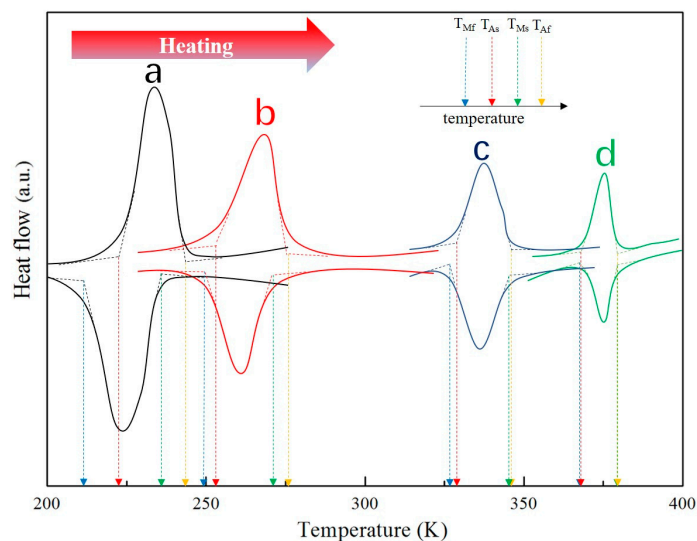


Figure 6. Differential scanning calorimeter (DSC) curve of $\text{Co}_{33}\text{Ni}_{31}\text{Al}_{27}\text{Fe}_9$ alloy with furnace cooled and RS: (a) furnace cooled; (b) D8; (c) D4; and (d) D1.

Furthermore, an apparent thermal hysteresis was observed during the heating and cooling process. The thermal hysteresis value (ΔT) can be calculated by the equation: $\Delta T = T_{As} - T_{Mf}$. The values of thermal hysteresis equaled approximately 11.8, 4.5, 2.3, and 0.7 K for furnace cooled sample, D8, D4, and D1, respectively. The width of the thermal hysteresis, which presented a continuous reduction, may be caused by the change of the elastic and surface energies during martensitic transformation with the rising R_C value [22].

In recent reports, Sanchez et al. [23] and Jia et al. [24] indicated that the martensitic transformation temperature in Housler alloys proved to be very sensitive to the valence electron concentration ($R_{e/a}$). In dual-phases structure MCMEA, only the ferromagnetic twin martensitic can obtain the MFIS by EMF, while the γ cannot participate in this process. The element distribution of β phase or martensite has clear distinction with different R_C value. Hence, to illustrate the reason of martensitic transformation temperature change, the $R_{e/a}$ value of β phase and martensite can be calculated by Equation (1), and the results are illustrated in Figure 7.

$$R_{e/a} = \sum(a_i \times b_i) \quad (2)$$

where, a_i and b_i correspond to the atomic valence electron and the proportion of element i , respectively. The atomic valence electron for Co, Ni, Al and Fe were 9, 10, 3 and 8, respectively.

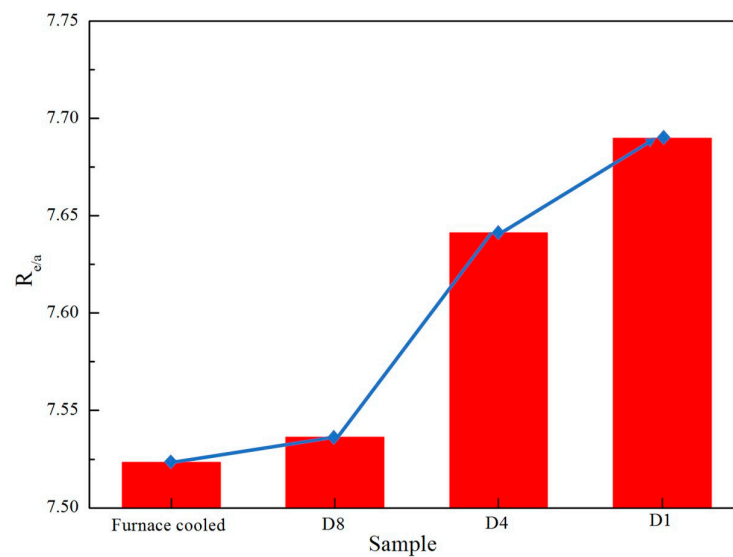


Figure 7. $R_{e/a}$ of $\text{Co}_{33}\text{Ni}_{31}\text{Al}_{27}\text{Fe}_9$ alloy with furnace cooled and RS.

According to Figure 7, it is concluded that the $R_{e/a}$ value of martensite in $\text{Co}_{33}\text{Ni}_{31}\text{Al}_{27}\text{Fe}_9$ alloy had a significant increasing tendency as the R_C was rising. For the furnace cooled sample, the R_C value is the minimum when compared with RS sample and the $R_{e/a}$ value, which was calculated from the element content, corresponded to the minimum also. By raising the R_C value, the $R_{e/a}$ value initially slightly increased (from furnace cooled rise to $62.5 \text{ K}\cdot\text{s}^{-1}$), and subsequently increased rapidly (from $62.5 \text{ K}\cdot\text{s}^{-1}$ rise to $250 \text{ K}\cdot\text{s}^{-1}$), while at the last stage it increased slowly (from $250 \text{ K}\cdot\text{s}^{-1}$ rise to $4000 \text{ K}\cdot\text{s}^{-1}$). An explanation of this “slow-rapid-slow” rising phenomenon can be ascribed to the element distribution of alloy including R_C value effects similar to the analysis in the EDS part. This results in a satisfying agreement, with the report presented by Rekik et al. [22].

Another reason for martensitic transformation temperature and thermal hysteresis change is the distribution of elements changes. According to the RS process, the element content of Ni and Al in martensite consistently decreasing, but Co and Fe rising. Although the increase of Co content can result in the martensitic transition temperature decreasing, nevertheless, the rising of the Fe content and the decreasing of Ni and Al can greatly ascend the martensitic transition temperature and decrease the thermal hysteresis. So, the martensitic transition temperature keeps ascending and the thermal hysteresis reduces gradually during the RS process.

The morphology details and the structure of martensite of D4, and D1 was determined by TEM and SADP analysis (Figure 8). However, the lath-shaped martensite in both D4 and D1, contained numerous black and white stripes alternating presence, which exhibited a typical twinning structure. The twin martensite boundaries aligned at approximately $\pm 45^\circ$ including twin boundaries. Moreover, the SADP of the martensite twin structure along the [001] m zone axis in D4 and the [101] m zone axis in D1 had presented dual-sets of overlapping diffraction patterns (ODP), as illustrated in the top right corner in Figure 8. The dual-sets ODP in both D4 can be indexed by the $L1_0$ structure with $a = b = 0.382 \text{ nm}$, $c = 0.321 \text{ nm}$. Additionally, in D1, the ODP can be indexed by the $L1_0$ structure with $a = b = 0.376 \text{ nm}$, $c = 0.325 \text{ nm}$, which compromises with the XRD analysis.

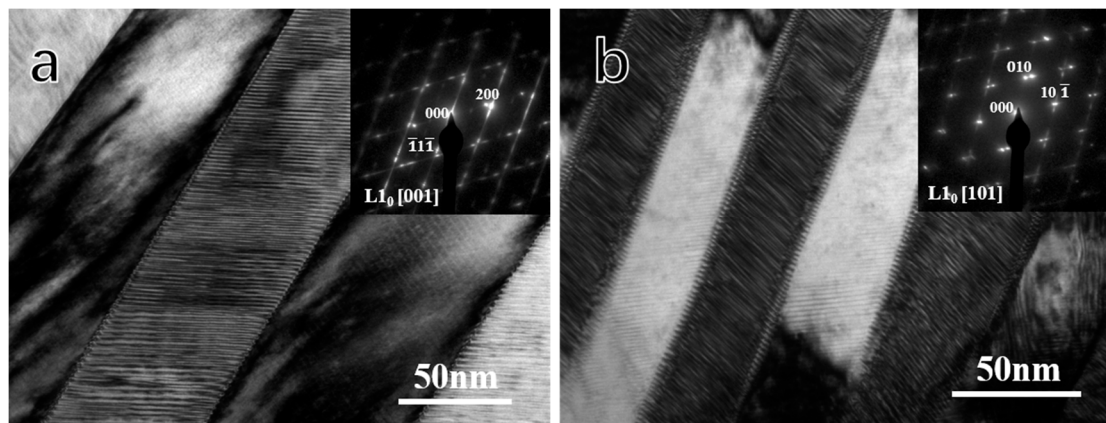


Figure 8. Transmission electron microscopy (TEM) micrograph and corresponding selected area electron diffraction patterns (SADP) of martensite: (a) D4; (b) D1.

4. Conclusions

In this paper, authors attempted to reveal the structure and martensitic transition change during the RS process. Thus, the changes of martensite structure, martensitic transformation temperature, and the thermal hysteresis during the rapidly solidified process were investigated in detail and the main conclusions are as follows:

- (1) The microstructure of $\text{Co}_{33}\text{Ni}_{31}\text{Al}_{27}\text{Fe}_9$ alloy with furnace cooled and RS corresponded to a dual-phase structure, β phase + γ phase in furnace cooled sample, and D8; martensite + γ phase in D4 and D1. The γ phase at the grain boundaries tended to be limited and more fragile, when the R_C value was raised.
- (2) By increasing the R_C value, the elements Co and Fe in Co-rich γ phase presented apparent trend diffusion to the β phase and martensite.
- (3) The martensite structure of D4 corresponded to the $L1_0$ structure with $a = b = 0.382$ nm, $c = 0.321$ nm and in D1, the martensite equaled the $L1_0$ structure with $a = b = 0.376$ nm, $c = 0.325$ nm.
- (4) The one-step austenite-martensite phase transformation occurred during the process of heating and cooling. The phase transition temperature preserved a significant tendency of increasing with the rise of the R_C value, even over the room temperature in D1. Additionally, the values of thermal hysteresis were about 11.8, 4.5, 2.3, and 0.7 K for furnace cooled sample, D8, D4, and D1, respectively.

Acknowledgments: This work is supported by the Scientific Foundation of Nanjing Institute of Technology (Project No. YKJ201504), the Opening Project of Jiangsu Key Laboratory of Advanced Structural Materials and Application Technology (Project No. ASMA201609), the Natural Science Foundation of Jiangsu Province of China (Project No. BK20160869), Basic research project of Nanjing Institute of Technology (Project No. JCYJ201605), the National Natural Science Foundation of China (Project No. 61175069) and Outstanding Scientific and Technological Innovation Team in Colleges and Universities of Jiangsu Province.

Author Contributions: Jia Ju, Ligu Shuai and Huiling Chen conceived and designed the experiments; Huan Liu, Ligu Shuai and Huiling Chen performed the experiments; Huan Liu, Chen Yan and Zhuang Liu contributed materials; Ligu Shuai, Huiling Chen and Huan Liu analyzed the data; Jia Ju, Ligu Shuai and Huiling Chen wrote the paper. All authors have discussed the results, read and approved the final manuscript.

Conflicts of Interest: The authors declare no conflict of interest.

References

1. Zhou, L.; Schneider, M.M.; Giri, A.; Cho, K.; Sohn, Y. Microstructural and crystallographic characteristics of modulated martensite, non-modulated martensite, and pre-martensitic tweed austenite in Ni-Mn-Ga alloys. *Acta Mater.* **2017**, *134*, 93–103. [[CrossRef](#)]
2. Dai, Y.C.; Hou, L.; Fautrelle, Y.; Li, Z.B.; Esling, C.; Ren, Z.M.; Li, X. Martensitic transformation and detwinning in directionally solidified two-phase Ni-Mn-Ga alloys under uniaxial compression. *J. Alloys Compd.* **2017**, *722*, 721–728. [[CrossRef](#)]
3. Mino, J.; Ipatov, M.; Gamcova, J.; Saksl, K.; Durisin, M.; Zhukova, V.; Vargova, Z.; Zhukov, A.; Varga, R. Magnetic Characterization of Melt-Spun Co-Ni-Ga Ferromagnetic Superelastic Alloy. *Acta Phys. Pol. A* **2017**, *131*, 1075–1077. [[CrossRef](#)]
4. Vollmer, M.; Krooss, P.; Segel, C.; Weidner, A.; Paulsen, A.; Frenzel, J.; Schaperc, M.; Eggeler, G.; Maier, J.H.; Niendorfa, T. Damage evolution in pseudoelastic polycrystalline Co-Ni-Ga high-temperature shape memory alloys. *J. Alloys Compd.* **2015**, *633*, 288–295. [[CrossRef](#)]
5. Timofeeva, E.E.; Panchenko, E.Y.; Chumlyakov, Y.I.; Maier, H.J.; Gerstein, G. Peculiarities of High-Temperature Superelasticity in Ni-Fe-Ga Single Crystals in Compression. *Tech. Phys. Lett.* **2017**, *43*, 320–323. [[CrossRef](#)]
6. Chabungbam, S.; Borgohain, P.; Ghosh, S.; Singh, N.; Sahariah, M.B. Martensitic transformation and magnetism in Ni and Fe-rich compositions of Ni-Fe-Ga shape memory alloys. *J. Alloys Compd.* **2016**, *689*, 199–207. [[CrossRef](#)]
7. Sharma, J.; Suresh, K.G. Investigation of multifunctional properties of $Mn_{50}Ni_{40-x}Co_xSn_{10}$ ($x = 0-6$) Heusler alloys. *J. Alloys Compd.* **2015**, *620*, 329–336. [[CrossRef](#)]
8. Liu, J.; Fei, X.P.; Gong, Y.Y.; Xu, F. Phase Transition and Magnetocaloric Properties of $Ni_{50}Mn_{35-x}In_{15}Cu_x$ Bulk Alloys and Ribbons. *IEEE Trans. Magn.* **2015**, *51*, 2503004. [[CrossRef](#)]
9. Ju, J.; Yang, L.; Hao, S.; Mao, Q.T.; Lou, S.T.; Liu, H. Microstructure Martensite Transition and Mechanical Properties Investigations of Polycrystalline Co-Ni-Al Alloys with Er Doping. *J. Mater. Eng. Perform.* **2017**, *26*, 1062–1068. [[CrossRef](#)]
10. Yamakov, V.; Hochhalter, J.D.; Leser, W.P.; Warner, J.E.; Newman, J.A.; Pun, G.P.P.; Mishin, Y. Multiscale modeling of sensory properties of Co-Ni-Al shape memory particles embedded in an Al metal matrix. *J. Mater. Sci.* **2016**, *51*, 1204–1216. [[CrossRef](#)]
11. Li, P.Z.; Karaca, H.E.; Chumlyakov, Y.I. Orientation dependent compression behavior of $Co_{35}Ni_{35}Al_{30}$ single crystals. *J. Alloys Compd.* **2017**, *718*, 326–334. [[CrossRef](#)]
12. Kokorin, V.V.; Konoplyuk, S.M.; Dalinger, A.; Maier, H.J. Influence of martensitic transformation on the magnetic transition in Ni-Mn-Ga. *J. Magn. Magn. Mater.* **2017**, *432*, 266–270. [[CrossRef](#)]
13. Oikawa, K.; Wulff, L.; Iijima, T.; Gejima, F.; Ohmori, T.; Fujita, A.; Fukamichi, K.; Kainuma, R.; Ishida, K. Promising ferromagnetic Ni-Co-Al shape memory alloy system. *Appl. Phys. Lett.* **2001**, *79*, 3290–3292. [[CrossRef](#)]
14. Ju, J.; Lou, S.T.; Yan, C.; Yang, L.; Li, T.; Hao, S.; Wang, X.Y.; Liu, H. Microstructure Magnetism and Magnetic Field Induced-Strain in Er-Doped Co-Ni-Al Polycrystalline Alloy. *J. Electron. Mater.* **2017**, *46*, 2540–2547. [[CrossRef](#)]
15. Ju, J.; Xue, F.; Li, H. Microstructure and Magnetic Property Variation with Addition of Rare Earth Element Dy in Co-Ni-Al Ferromagnetic Shape Memory Alloy. *J. Iron Steel Res. Int.* **2015**, *22*, 858–863. [[CrossRef](#)]
16. O’Handley, R.C. Model for strain and magnetization in magnetic shape-memory alloys. *J. Appl. Phys.* **1998**, *83*, 3263–3270. [[CrossRef](#)]
17. Olszewski, J.; Zbrozczyk, J.; Hasiak, M.; Kaleta, J.; Nabialek, M.; Bragieli, P.; Sobczyk, K.; Ciurzyńska, W.; Świerczek, J.; Łukiewska, A. Microstructure and magnetic properties of Fe-Co-Nd-Y-B alloys obtained by suction casting method. *J. Rare Earths* **2009**, *27*, 680–683. [[CrossRef](#)]
18. Ju, J.; Xue, F.; Sun, L.X. Effect of Rapid Solidification on the Microstructure and Magnetic-Field-Induced Strain of $Co_{1.36}Ni_{1.21}AlFe_{0.12}$. *Mater. Manuf. Process.* **2015**, *30*, 637–643. [[CrossRef](#)]
19. Zhou, T.; Yang, M.B.; Zhan, J.; Peng, C.Y.; Hu, J.J.; Chen, K.; Zhou, Z.; Chen, Z.H. Investigation on the Microstructure Characterization and Aging Response of Rapidly Solidified Mg-6wt%Zn-5wt%Ca Alloy Produced by Atomization-Twin Roll Quenching Technology. *Mater. Manuf. Process.* **2012**, *27*, 125–129. [[CrossRef](#)]

20. Liu, J.; Li, J.G. Microstructure, shape memory effect and mechanical properties of rapidly solidified Co-Ni-Al magnetic shape memory alloys. *Mater. Sci. Eng. A* **2007**, *454*, 423–432. [[CrossRef](#)]
21. Lin, X.H.; Johnson, W.L. Formation of Ti-Zr-Cu-Ni bulk metallic glasses. *J. Appl. Phys.* **1995**, *78*, 6514–6519. [[CrossRef](#)]
22. Rekik, H.; Krifa, M.; Bachaga, T.; Escoda, L.; Sunol, J.J.; Khitouni, M.; Chmingui, M. Structural and martensitic transformation of MnNiSn shape memory alloys. *Int. J. Adv. Manuf. Technol.* **2017**, *90*, 291–298. [[CrossRef](#)]
23. Sanchez-Alarcos, V.; Recarte, V.; Perez-Landazabal, J.I.; Gomez-Polo, C.; Rodriguez-Velamazan, J.A. Role of magnetism on the martensitic transformation in Ni-Mn-based magnetic shape memory alloys. *Acta Mater.* **2012**, *60*, 459–468. [[CrossRef](#)]
24. Ju, J.; Lou, S.T.; Yang, L.; Li, T.; Hao, S.; Yan, C. Effect of Electronic and Magnetic Valences on Phase Transition and Magnetic Properties in Co-Ni-Al-RE (RE = Gd, Dy and Er) Alloys. *J. Electron. Mater.* **2017**, *46*, 1390–1395. [[CrossRef](#)]



© 2017 by the authors. Licensee MDPI, Basel, Switzerland. This article is an open access article distributed under the terms and conditions of the Creative Commons Attribution (CC BY) license (<http://creativecommons.org/licenses/by/4.0/>).